Physics of Fluids

RESEARCH ARTICLE | OCTOBER 07 2024

Benchmark problems for simulating Hyperloop aerodynamics

Alex J. Lang ; David P. Connolly ; Gregory de Boer ; Shahrokh Shahpar ; Benjamin Hinchliffe;
Carl A. Gilkeson

Physics of Fluids 36, 106116 (2024)
https://doi.org/10.1063/5.0229914

AIP Publishing

Physics of Fluids ARTICLE pubs.aip.org/aip/pof

Benchmark problems for simulating Hyperloop aerodynamics

Cite as: Phys. Fluids **36**, 106116 (2024); doi: 10.1063/5.0229914
Submitted: 20 July 2024 · Accepted: 31 August 2024 ·
Published Online: 7 October 2024

Alex J. Lang,[1] David P. Connolly,[2] Gregory de Boer,[3] Shahrokh Shahpar,[4] Benjamin Hinchliffe,[5] and Carl A. Gilkeson[5,a)]

AFFILIATIONS

[1]EPSRC CDT in Fluid Dynamics, University of Leeds, Leeds LS2 9JT, United Kingdom
[2]Institute for High Speed Rail and System Integration, School of Civil Engineering, University of Leeds, Leeds LS2 9JT, United Kingdom
[3]Institute of Thermofluids, School of Mechanical Engineering, University of Leeds, Leeds LS2 9JT, United Kingdom
[4]Department of Aeronautics, Imperial College London, London SW7 2AZ, United Kingdom
[5]Aerospace Industrial Advisory Board, School of Mechanical Engineering, University of Leeds, Leeds LS2 9JT, United Kingdom

a)**Author to whom correspondence should be addressed:** c.a.gilkeson@leeds.ac.uk

ABSTRACT

Hyperloop is proposed as the next generation of sustainable high-speed transport. Recently, an increasing body of literature has been amassed on Hyperloop aerodynamics, however, the vast majority of this work is numerical. Experimentally, there are few relevant studies and none are suitable for validating computational approaches. This paper presents three benchmark cases to provide a framework for computational research and to address this significant gap. Benchmark 1 provides experimental data from existing work on a projectile traveling at Mach 1.1 in ground effect. This incorporates many of the flow characteristics of a Hyperloop system, including (i) transonic Mach numbers, (ii) wall confinement, and (iii) shock formation/reflection. These experimental data are compared to Computational Fluid Dynamics simulations with a very good match seen. Next, Benchmark 2 is proposed which extends these simulations toward a baseline Hyperloop pod design operating in an axisymmetric low-pressure tube environment. This is achieved in stages by adding a full tube, scaling up the domain, reducing the air pressure, and introducing a baseline pod design. It is shown that the enclosed tube environment causes the most significant change in aerodynamic characteristics via flow choking. Nevertheless, a number of aerodynamic similarities remain, compared to Benchmark 1. Finally, Benchmark 3 is proposed to explore the impact of ground clearance of the pod. This aspect has a significant influence on the flow by deflecting the wake and the downstream shock pattern. Furthermore, the drag, downforce, and pitching moment are all found to increase with lower ground clearances.

NOMENCLATURE

C_D	Drag coefficient
C_f	Friction coefficient
C_L	Lift coefficient
C_p	Pressure coefficient
CFD	Computational fluid dynamics
d	Body diameter, m
dt	Timestep, s
h	Ground clearance, m
l	Body length, m
M	Mach number
p	Pressure, Pa
R	Specific gas constant, J/(kg K)
Re	Reynolds number
RANS	Reynolds-Averaged Navier–Stokes
r	Mesh refinement ratio
s	Shock stand-off distance, m
t	Time, s
T	Temperature, K
$\mathbf{u}$	Velocity, m/s
β	Blockage ratio
γ	Specific heat ratio

μ	Dynamic viscosity, Pa s
ρ	Density, kg/m^3
$\boldsymbol{\omega}$	Vorticity, 1/s

I. INTRODUCTION

The Hyperloop concept aims to achieve sustainable rapid travel by transporting passengers in pods through a tube system under near-vacuum conditions. The low air density will reduce aerodynamic drag on the pods, which should allow higher speeds and lower energy consumption compared to conventional trains. Understanding the aerodynamics of such a system is a difficult challenge, as Hyperloop sits in an unconventional flow regime which combines transonic speeds, low air pressure, and a fully confined tube environment.[1] Hyperloop aerodynamics has been the topic of a significant amount of research as interest in the concept has grown in recent years.

The most important consideration in Hyperloop aerodynamics is the occurrence of choked flow. This describes the state in which the flow through the narrowest gap around the pod is sonic. If this is the case, the mass flow past the pod is limited and air accumulates upstream. This can dramatically increase the drag experienced by the pod and a normal shock will be generated which travels upstream.[2] An illustration of the predicted flow characteristics for a Hyperloop operating in a choked condition is shown in Fig. 1. The isentropic and Kantrowitz limits, which are derived from 1D theory,[3] provide upper and lower bounds on the pod speeds for which choked flow occurs. The range of choked flow speeds depends on the blockage ratio of the system, as shown in Fig. 2. For realistic blockage ratios ($\beta \approx 0.1$–0.4), it can be seen that the flow is predicted to be choked across most of the proposed Mach number range for a Hyperloop pod ($M \approx 0.5$–1.5).

The majority of the research on Hyperloop aerodynamics has involved numerical simulations,[1] covering aspects including the flow states,[4,5] shock characteristics,[2] transient properties,[6,7] and pod design.[8–10] Theoretical studies of Hyperloop aerodynamics have also been performed,[3] which mainly involve 1D analysis of the flow. Numerical results have been found to be in good agreement with the 1D theory in terms of predictions for the different expected flow states in a Hyperloop system.[2–4]

Very little experimental data on Hyperloop-type systems are available in the literature. This is a result of the difficulty in achieving transonic speeds with near-vacuum conditions in a high blockage ratio tube.[1] The only Hyperloop-specific results are given by Seo *et al.*,[11] who created a 1/15th scale Hyperloop model which was propelled at speeds up to 320 m/s (Mach 0.9). The focus of their research was on the leading shock wave behavior of the system, which they monitored using surface pressure measurements on the tube walls. Their experimental results were generally in agreement with previous theoretical and numerical predictions in the literature. However, these initial results are too limited in scope to be able to perform detailed validation of numerical simulations, and so a notable gap in knowledge remains.

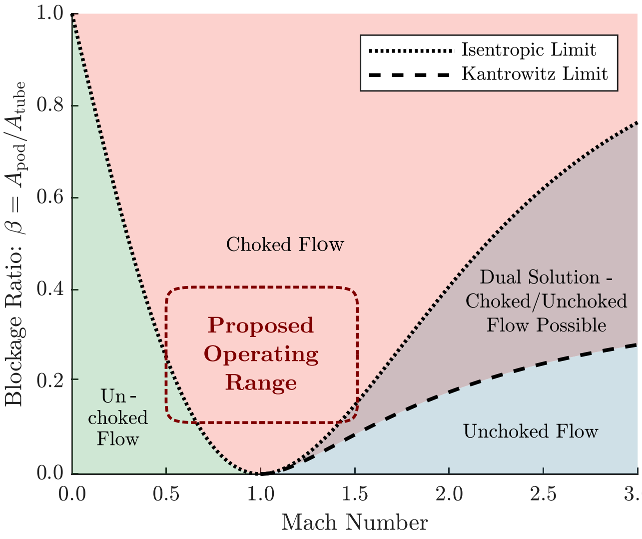

FIG. 2. The flow states in a Hyperloop system depending on the blockage ratio and Mach number.[1] The isentropic and Kantrowitz limits provide the bounds between the choked and unchoked states.

Most numerical studies in the literature have used related experimental cases for their validation that contain one or more of the flow characteristics expected in a Hyperloop system. This includes systems such as hypersonic intakes,[12–14] scramjet combustion chambers,[15–17] model trains,[18] and supersonic flow around axisymmetric bodies.[19] A summary of the most common validation cases used in the Hyperloop literature can be found in Lang *et al.*[1] The issue with the majority of these validation cases is that they each have one or more flow characteristics that are very different to those predicted for Hyperloop, such as notably different geometries, Reynolds numbers, or flow speeds. Therefore, a new approach is required to resolve this problem.

In a simplified sense, the Hyperloop system closely resembles the case of a projectile traveling at transonic speeds confined by solid walls. It is therefore proposed here that this would provide a more representative validation case, which can be readily adapted into a Hyperloop simulation.

Projectiles have been used as a validation case for a small number of Hyperloop numerical studies,[20,21] however in these cases the

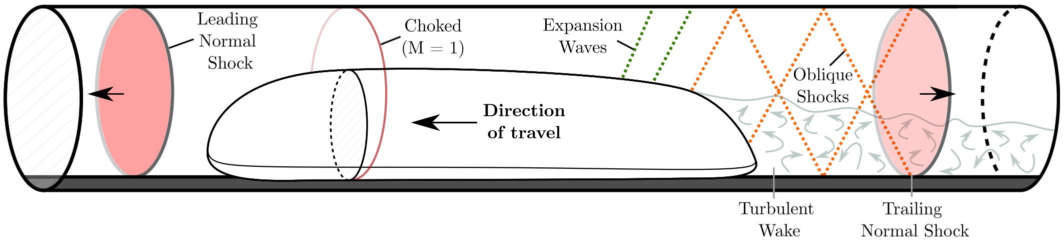

FIG. 1. Expected characteristics of fully developed choked flow in a Hyperloop system.[1] Not to scale.

projectile is moving in free air,[22] and so the effects of wall-proximity and reflecting shocks are not observed.

The literature on confined projectiles is sparse. To the authors' knowledge, Hruschka and Klatt[23] published the only investigation of fully confined projectile aerodynamics at a blockage ratio relevant to Hyperloop. They conducted experiments looking at a transonic ($M = 0.5 - 1.5$) 4.5 mm air gun style pellet, both in free-flight and inside a tube with a 28% blockage ratio. They measured aerodynamic drag, shock characteristics, and tube-wall surface pressures. Two-dimensional CFD simulations were also performed, using a sliding mesh method and the SST $k - \omega$[24] turbulence model. Their simulations were able to accurately reproduce the experimental drag results and allowed for analysis of the expected flow regimes for the projectile.

A small number of studies have been performed for projectiles that are wall-bounded on one side, as would be the case when fired close to the ground. The general idea of transonic and supersonic wall-confined aerodynamics, or more specifically "ground effect" aerodynamics, is of huge importance in a number of applications. Doig[25] gave a comprehensive review of this area, which includes discussion of ground effect in relation to high-speed trains. Further work carried out by the same research group led to notable studies of projectiles in ground effect.[26–30] They conducted live firing experiments, wind tunnel testing, and performed CFD simulations to analyze the flow generated by a projectile at a variety of transonic/supersonic speeds and ground separation distances. Extensive results and data are presented in these studies, including projectile surface pressure measurements and schlieren images of the shock formation which can be used for validating CFD results. Therefore, these studies are used as the basis for the benchmark cases in this paper, which are presented below.

II. BENCHMARK 1—GROUND-EFFECT PROJECTILE (B1)

The experimental and numerical results of Doig *et al.*[27] Young *et al.*,[28] Kleine *et al.*,[29] and Sheridan *et al.*[30] are suitable as an initial benchmark which presents a validation case for Hyperloop simulations. The flow speed in their experimental case is at Mach 1.1, which is within the speed regime proposed for Hyperloop, while the ground separation distance, h, is half of the projectile diameter, d. Based on the projectile diameter, the Reynolds number of the flow in the study is 1.1×10^6, which is approximately a factor of 10 higher than would be expected for a Hyperloop. Validating the CFD methodology against this case allows for an assessment of the accuracy in simulating the compressible flow features of a typical Hyperloop system. This includes resolving the expected shocks that the pod will generate, along with the wall interaction and shock reflection behavior.

In their original investigations,[27,29,30] surface pressure on the projectile was measured experimentally in a wind tunnel for free-air and $h/d = 0.5$ cases at Mach 1.1. Schlieren images were captured for various other Mach numbers and ground clearances to visualize the flow characteristics in the wind tunnel tests and also in live firing tests of the projectile. An example of these outputs and the experimental setup is shown in Fig. 3. Note that in the live firing tests, the projectile was spinning, and in the wind tunnel setup two models were used to create a symmetry condition, which is discussed in the following.

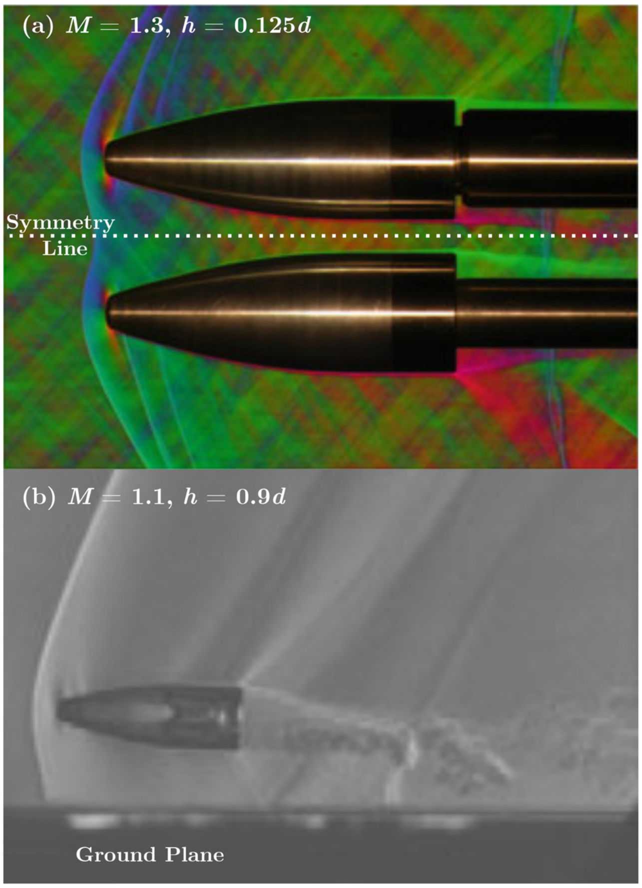

FIG. 3. (a) Schlieren results from the wind tunnel tests by Sheridan *et al.*[30] Reproduced with permission from Sheridan *et al.*, in Proceedings of the 30th International Symposium on Shock Waves 1 (Springer International, 2017), pp. 635–640. Copyright 2017 Springer International Publishing AG. Colors indicate the direction of the density gradient.[30,31] (b) Schlieren image of the live firing tests by Kleine *et al.*[29] Reproduced with permission from Kleine *et al.*, in 28th International Symposium on Shock Waves (Springer-Verlag, 2012), pp. 519–524. Copyright 2012 Springer-Verlag Berlin Heidelberg. Note that the projectile is spinning in this case.

A. Ground modeling

In the experiments by Doig *et al.*,[27] a symmetry method was used in which two nominally identical models were placed with a separation of twice the required ground clearance, which is equivalent to having a no-shear-stress ground plane.[32] The two models are shown in Fig. 3(a), where it can be seen that there are differences in the sting geometry, likely due to one of the models being instrumented for pressure and force measurements.

The symmetry method is often used to avoid difficulties in accurately capturing the relative motion of the wall in wind tunnel tests.[25,33] To be fully representative of a fired projectile, a moving-ground test can also be used which has the ground plane translating at the absolute speed of the body in the streamwise direction. This is extremely difficult to achieve practically at transonic speeds, but it is simple to implement in CFD studies.

B. Domain and boundary conditions

A quarter-cylinder geometry was produced for the simulation domain, with a vertical symmetry plane used to reduce the mesh size.

The projectile geometry was removed from the fluid domain and no-slip walls were applied to the resulting surfaces, as seen in Fig. 4. To match the physical experiments, the ground was modeled with a symmetry plane. The ground clearance was $h = 0.5d$ for the main ground effect simulation case. An additional free-air case was produced by modeling a quarter of the projectile centered on the axis of the quarter-cylinder domain. Domains with ground clearances of $h = 0.25d$, $0.75d$, and $1d$ were also created to measure the effect on shock stand-off distance.

A more realistic ground model was also tested to compare to the symmetry method. To achieve this, a no-slip condition was applied to the ground plane which was translated at the same velocity as the inlet flow. It was found that the resulting lift and drag forces on the projectile changed by less than 2% compared to simulations with a symmetry plane. Clearly, the symmetry method does a satisfactory job of producing realistic wall interaction, and the boundary layer effects on the wall are practically insignificant.

The other boundaries were modeled with far-field (characteristic) pressure conditions[34,35] at Mach 1.1 to match the experimental conditions. The turbulent intensity at the far-field boundaries is taken as 0.05%, as in the numerical studies of Doig *et al.*[27] They noted that this may be artificially low; however, higher turbulence levels were not found to substantially alter the pressure distributions on the projectile. The air in the system is modeled as an ideal gas and the 3 coefficient Sutherland's law[36] is used to account for the dependence of viscosity on temperature. The operating pressure in the simulation is 1 atm, matching the experimental case.

A summary of the domain sizings and boundary conditions is shown in Fig. 4. To verify that the results were independent of the placement of the far-field boundary, a simulation was performed with the domain size increased by a factor of 1.5 in each direction. The aerodynamic forces changed by less than 0.5%, confirming negligible sensitivity of the numerical results to the size of the domain.

C. Projectile geometry

The geometry is based on a Nosler 50 gr S.H.O.T projectile,[27] which was scaled up by a factor of 7.5 to assist with instrumenting the wind tunnel model. The final dimensions were $l = 120$ and $d = 42.6$ mm.

The exact geometry of the projectile used in the experiments and CFD simulations[27] could not be retrieved by the original authors, so this had to be approximated using inverse-design based on the pressure coefficient profiles. A parametric geometry consisting of tangentially connected arcs and straight sections was produced which visually matched the outline of the experimental geometry [Fig. 5(a)]. From here, 2D axisymmetric simulations were performed with iterative changes to the parameters in order to match the pressure profiles from the free-air experimental/numerical results. Once the geometry was finalized in 2D, this was simulated in 3D to verify the match before proceeding with the ground effect cases. Comparison of this geometry to the free-air experimental and numerical results of Doig *et al.*[27] is given in Fig. 5, along with the final geometry parameters. Very close agreement with the original pressure profiles is seen; this will be discussed in further detail in Sec. II F.

D. Meshing

Poly-hexcore meshes were used for all simulations. This method uses structured hexahedral blocks in the bulk of the domain, away from the boundaries, which aligns the gridlines with the free-stream flow, thereby minimizing numerical diffusion. Inflation layers were used to generate structured blocks of prism cells around the projectile, with clustering toward the surface to resolve the boundary layer. Polyhedral cells were then generated to fill the domain between the structured blocks, the boundaries, and the inflation layer summit. Inevitably, the presence of polyhedral cells in the domain will add greater numerical diffusion, compared to hexahedra. However, these regions are represented in relatively small volumes within the domain, and their presence is an intrinsic part of this meshing method. Overall, the poly-hexcore method allows rapid generation of meshes for complex geometries, while maintaining the benefit of being largely aligned with the flow direction in the structured regions. Areas of high element density were applied in regions with strong expected flow gradients, such as the nose, corner, and wake of the projectile.

Adaptive refinement was used to further increase the resolution of the mesh in the regions where shocks and expansions occur. The procedure for adaption was to refine cells with static pressure gradient values in the top 90%. This adaption and the overall structure of the mesh can be seen in Fig. 6.

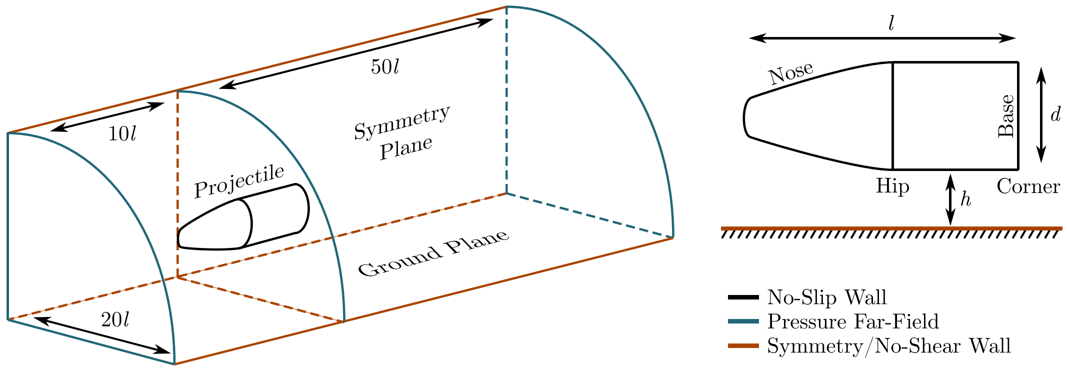

FIG. 4. Domain and boundary conditions for the CFD simulations of Benchmark 1, the transonic projectile in ground effect, matching the case of Doig *et al.*[27] $l = 120$ and $d = 42.6$ mm. Not to scale.

(a)

Symbol	Radius (mm)	Centre Coordinate	
		x (mm)	y (mm)
R1	28.8	28.800	0.000
R2	4.5	4.645	2.649
R3	290	96.286	-267.743
R4	30	74.000	-8.700

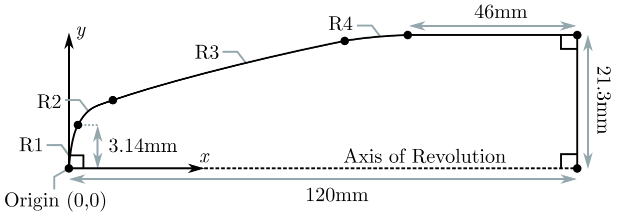

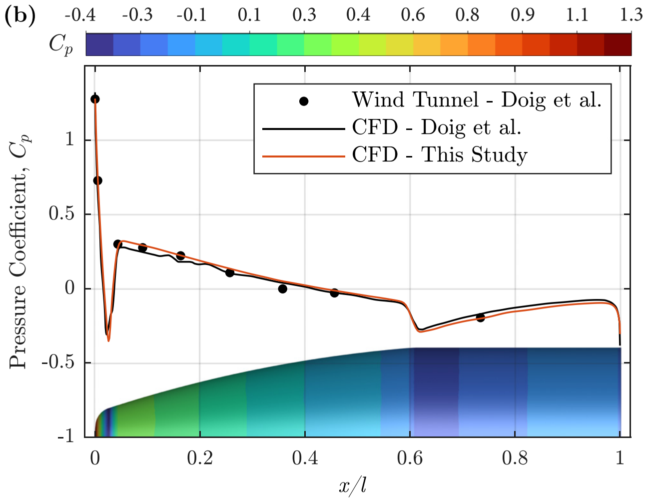

FIG. 5. (a) Final projectile geometry consisting of tangent arcs and straight sections (not to scale). Coordinates for the geometry are also included in the supplementary dataset. (b) Comparison between the surface pressure profiles for this geometry and the results of Doig *et al.*[27] in the free-air case.

A mesh independence study was performed for the ground clearance $h/d = 0.5$ case. A series of 4 meshes with a refinement ratio $r \approx 1.4$ were used. Though each size specification for the mesh was systematically altered by this refinement ratio, the overall ratio varies slightly as the mesh is unstructured in places. Both C_L and C_D were calculated for each simulation at the different refinement levels and are shown in Fig. 7. The 10.6M element mesh (shown in Fig. 6) was determined to be sufficiently refined, with force values within 1% of the most refined mesh. The average wall y^+ value on the projectile surface (excluding the base where the flow is separated) is 0.72. This mesh design strategy was used for the final results and also as the baseline to generate the mesh for the subsequent Hyperloop simulations.

E. Solver settings and turbulence modeling

The simulations were performed using Ansys Fluent 2020R2,[37] which is a general purpose finite-volume solver. The governing equations for the simulations are the compressible Navier–Stokes equations,[38]

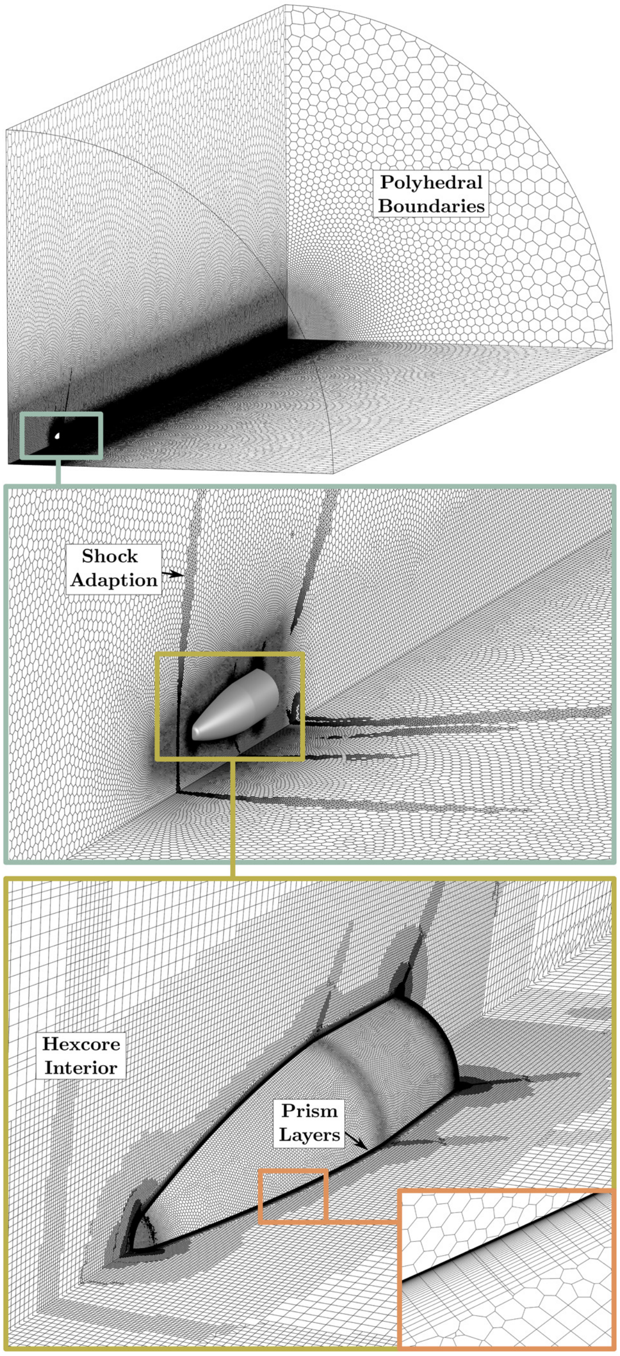

FIG. 6. Final 10.6 M element poly-hexcore mesh for the projectile simulations with adaptive refinement in regions with high static pressure gradient.

$$\frac{\partial \rho}{\partial t} + \nabla(\rho \mathbf{u}) = 0, \tag{1}$$

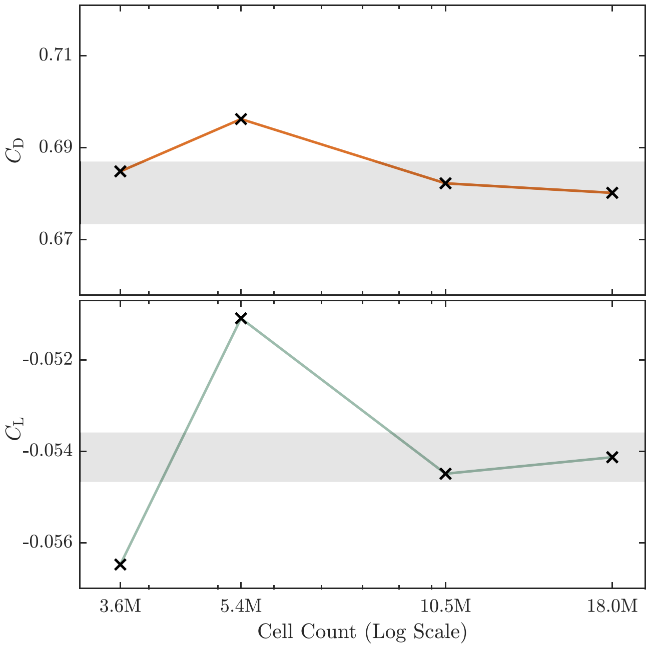

FIG. 7. Lift and drag coefficient for the mesh independence study of the projectile simulations with $h = 0.5d$. The refinement ratio between meshes was approximately $r = 1.4$. The gray shaded regions show ±1% intervals around the values for the most refined mesh.

$$\frac{\partial(\rho u)}{\partial t} + \nabla(\rho u \mathbf{u}) = -\frac{\partial p}{\partial x} + \nabla(\mu \nabla u), \tag{2}$$

$$\frac{\partial(\rho v)}{\partial t} + \nabla(\rho v \mathbf{u}) = -\frac{\partial p}{\partial y} + \nabla(\mu \nabla v), \tag{3}$$

$$\frac{\partial(\rho w)}{\partial t} + \nabla(\rho w \mathbf{u}) = -\frac{\partial p}{\partial z} + \nabla(\mu \nabla w), \tag{4}$$

along with the ideal gas equation of state,

$$p = \rho R T. \tag{5}$$

Here, $\mathbf{u} = (u, v, w)$ is velocity, p is the pressure, ρ is the density, T is the temperature, μ is the dynamic viscosity, and R is the specific gas constant.

The steady-state, coupled, pressure-based version of the Ansys Fluent solver was used for the simulations. Second-order schemes were used for all discretizations and interpolations. The least squares cell-based method was used for gradient evaluations, which offers higher accuracy than the Green-Gauss cell-based method, as the mesh contains unstructured sections.

The Reynolds number of the flow based on the projectile length is approximately 3 000 000. This is significantly above the widely accepted range for low Reynolds number *aerodynamics* (<500 000[39]), suggesting that the flow will not be significantly influenced by transition effects. A Reynolds-averaged Navier–Stokes (RANS) method with the SST $k-\omega$ model[24] was deemed suitable for the simulations and was chosen so as to match the CFD methods used in the original study by Doig *et al.*[27] To verify that transition effects are negligible, a simulation of the final case was performed using the transition SST model.[40] No significant changes to the flow features were seen in comparison to the simulations with non-transitional models and the aerodynamic forces differed by $< 0.2\%$. This underlines the suitability of the SST $k-\omega$ model at this Reynolds number. Transition effects are considered later for the Hyperloop simulations in Sec. III B which are at a significantly lower Reynolds number.

F. Validation results and comparison to experiments

The Mach number profile for the ground effect projectile case is shown in Fig. 8. Due to the blunt nose geometry, a detached bow shock is generated off the front of the body. This shock curves with the flow above the projectile, however, due to the close ground proximity, it stays approximately normal to the flow between the projectile and the ground plane. Expansion waves are generated where the flow turns away from the free-stream direction at the hip and rear corner of the geometry. On the underside of the projectile, the expansions are reflected back toward the body by the ground plane. The presence of the reflecting expansions beneath the projectile forms a low-pressure region, causing the wake to be deflected downward. An oblique recompression shock is also generated where the flow returns to approximately free-stream conditions. The reflection of this recompression shock is particularly strong where it is confined between the ground plane and the wake. This is seen by the high density of isolines in Fig. 8.

The qualitative agreement between the simulated results here and the schlieren images of the experiments shown in Fig. 8 is good. The shape of the bow shock and separation distance from the projectile is consistent between the wind tunnel results and the simulations. The curvature of the bow shock is higher for the fired projectile, likely due to the fact that the geometry is 7.5 times smaller than in the other tests. The simulation captures the same downward deflection of the wake that is seen in the live firing results; however, this is not seen in the wind tunnel as the body is mounted on a sting. The characteristics of the oblique shock generation and reflection off the ground plane appear to be broadly consistent across the three schlieren images, with a slightly steeper angle observed in the wind tunnel results. This is likely to be caused by slight differences in the geometry at the base corner of the projectile and also the presence of the sting in the wind tunnel.

Figure 9 shows the surface pressure on the projectile along the upper and lower centerlines. The profile matches very closely with the experimental and numerical results of Doig *et al.*[27] A slight difference is seen in the two sets of numerical results on the underside of the projectile, near the base. This corresponds to the location at which the expansion wave generated at the mid-section of the projectile is reflected back from the wall and hits the surface. The results in this study show the disturbance caused by the reflected expansion leading to marginally less pressure recovery compared to the results of Doig *et al.*[27] However, no experimental data are available at this location for comparison. The marginal difference is likely to be caused by minor differences between the geometry, mesh, and numerical codes used in the original study[27] and the present study. The effect of this difference on the total lift prediction is likely to be negligible, though lift was not reported for the simulations by the original authors.

The drag coefficient of the projectile in the simulations is 0.68, with the base drag due to low pressure in the wake contributing 62%

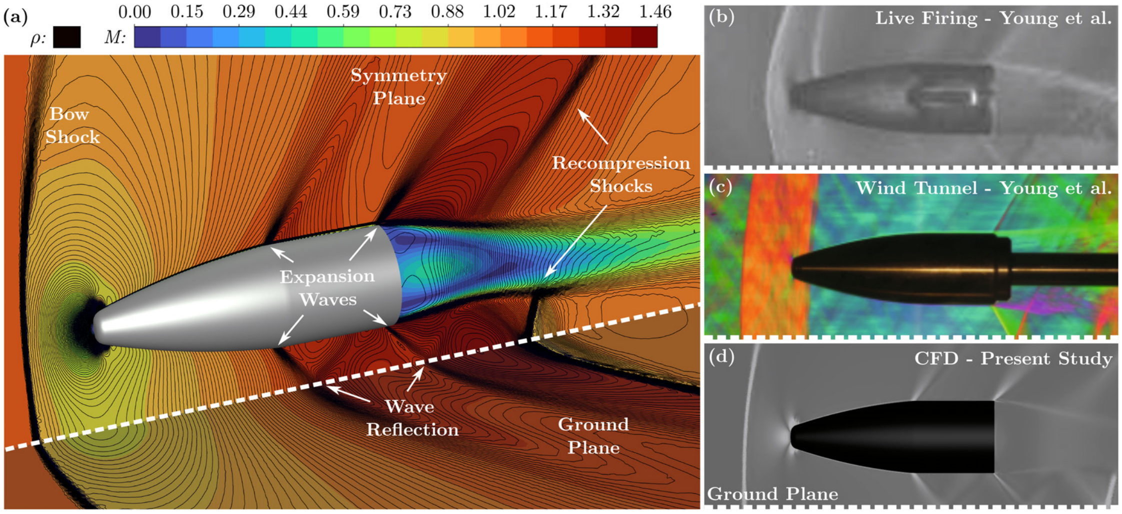

FIG. 8. (a) Contours of Mach number and isolines of density on the ground and symmetry planes for Benchmark 1, the projectile-in-ground-effect simulation. (b)–(d) Comparison of numerical schlieren (density gradient contour) from the present study with the experimental schlieren images of wind tunnel and live firing tests from Young *et al.*[28] Reproduced with permission from Young *et al.*, in 29th International Symposium on Shock Waves 2 (Springer International, 2015), pp. 1297–1302. Copyright 2015 Springer International Publishing Switzerland.

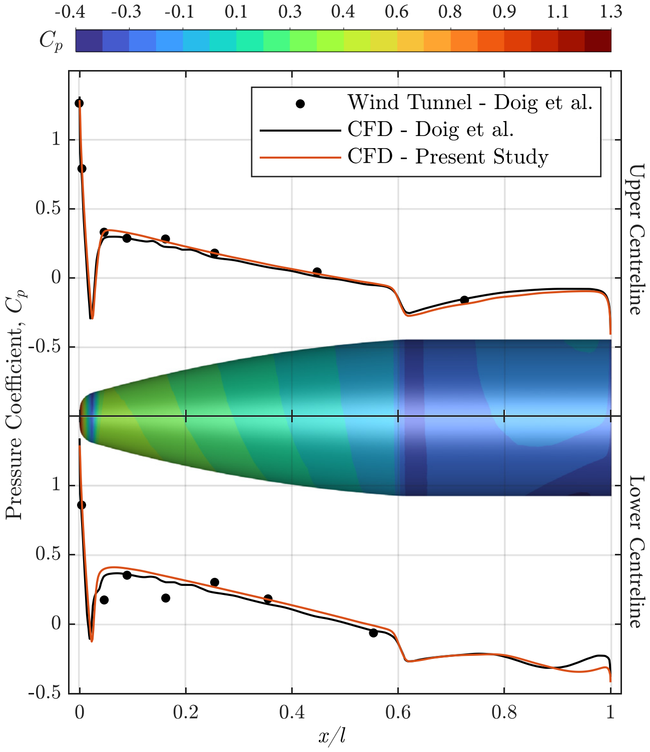

FIG. 9. Pressure coefficient contours on the projectile surface, along with profiles on the upper and lower centerlines with comparison to the experimental and numerical results of Doig *et al.*[27]

of the overall drag. Pressure drag is dominant and accounts for 95% of the total, while the remaining 5% is due to friction drag.

Figure 10 compares the bow shock stand-off distance, *s*, normalized with respect to projectile diameter, *d*, at different ground clearances for the simulations in the present study and the results of Doig *et al.*[27] For the simulations, *s* was measured as the horizontal distance between the front center point of the projectile and an isosurface of Mach 1, which approximates the shock surface.

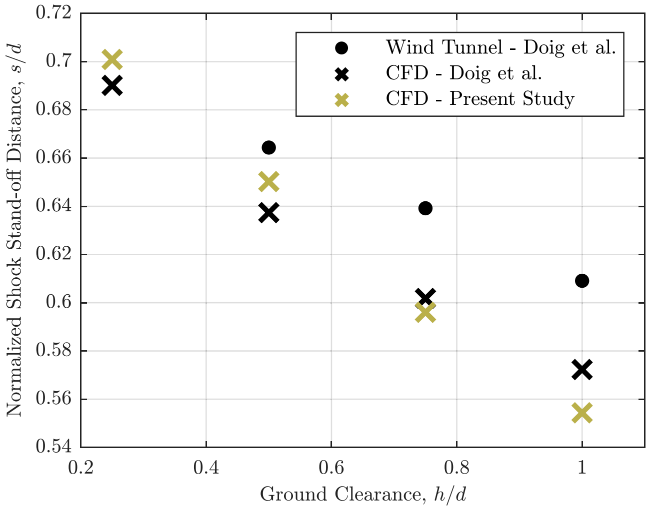

FIG. 10. Normalized shock stand-off distance, *s*/*d*, for the simulations in the present study, along with the numerical and experimental results of Doig *et al.*[27]

The normalized stand-off distance is seen to decrease with higher ground clearances in each set of results. In comparison to the wind tunnel results, s/d is under-predicted by both sets of CFD outputs. The gradient of the decrease is reasonably consistent between the experimental and numerical results from Doig *et al.*,[27] while the gradient of the results from the present study show a steeper decline. This could be due to slight differences in the curvature of the nose geometry used in the two studies (recall Sec. II C). Further sources of uncertainty include potential differences in ambient conditions which were not fully reported in the work of Doig *et al.*[27] Overall, a satisfactory match in the trends is observed, which gives further confidence that the modeling methods and the symmetry boundary conditions are capturing the physics of the real system.

III. BENCHMARK 2—BASELINE HYPERLOOP DESIGN (B2)

The transonic projectile validation case, Benchmark 1, is the basis for developing Benchmark 2, a generalized Hyperloop model simulation. This was constructed by successively making the following changes to the validated model while keeping all other variables and settings consistent:

1. enclosed tube,
2. increased scale,
3. decreased operating pressure, and
4. introduced pod geometry.

Following this logic, a simulation was performed after each stage in order to monitor the effect of the individual changes. The rationale for this procedure is to keep as close to the validated case as possible in order to maximize the confidence in the accuracy of the final Hyperloop simulations. A summary of the simulation parameters for each stage and the resulting drag outputs are given at the end of this section in Table I. A consistent flow speed of Mach 1.1 is used for all of the simulations, which matches the Benchmark 1 case.

The domain and boundary conditions are summarized in Fig. 11, with the only notable change from the validation case being that the ground plane is changed to a full tube, which is again modeled as a no-shear-stress wall. The mesh sizing controls relative to the domain size were also kept consistent with the projectile-in-ground-effect simulations. A slight exception to this was the inflation layer, which was scaled according to the Reynolds number. Figure 12 shows the mesh for the final Hyperloop model, which consists of 8.3 M cells. Mesh independence was confirmed in the same way as for Benchmark 1, and the drag coefficient was found to differ by less than 0.1% between the final mesh and a refined version with 17 M cells. The average wall y^+ value on the pod surface was found to be 0.37 for the final mesh.

The transition SST turbulence model, which combines the SST $k-\omega$ turbulence model with the $\gamma-\mathrm{Re}_\theta$ transition method,[40,41] is used for all of the following simulations in this section. This is in order to capture any transition effects that occur as the Reynolds number is altered by the ensuing scale and pressure changes (see Table I). The transition SST model has been validated for a wide variety of aerodynamic flows with significant transition effects.[41,42]

Subsections III A–III D describe the salient features of the results for each of the 4 successive steps in developing the Hyperloop model. In Sec. III D, the resulting simulation is then compared to the equivalent system running in free air, to assess the benefit of the low-pressure environment. Modeling of the transient features of the flow is also considered in Sec. III E, along with the effect of altering the ground clearance in Sec. IV.

A. Enclosed tube (B2a)

The first step in modifying the case into a Hyperloop system was to fully enclose the body within a tube. The tube surrounds the projectile centrally, such that the tube wall is positioned half a diameter from the body ($h = 0.5d$), which matches the separation from the ground plane in Benchmark 1. This produces an axisymmetric domain with the tube diameter being double that of the body, as shown in Fig. 11. The resulting blockage ratio is $\beta = 0.25$, which is consistent with values proposed in Hyperloop literature.[1,3,43,44] This enclosed tube geometry is designated B2a (see Table I).

The total enclosure of the body within a tube gives the most significant change to the flow characteristics. As discussed in the Introduction, flow choking is possible within an enclosed tube. For a pod speed of Mach 1.1 and blockage ratio of 0.25, Fig. 2 shows that the 1D isentropic theory predicts that the flow will indeed choke.

TABLE I. Summary of the parameters used for the simulations building from the wall-bounded projectile, B1, to the Hyperloop pod in the tube, B2c. These simulations are performed at Mach 1.1 to match Benchmark 1.

Fixed parameters

Temperature	Mach no.	Pod Velocity	Blockage ratio (full-tube)	Ground separation (h)	Turbulence model
300 K	1.1	381 m/s	0.25	0.5d	Transition SST

Varying parameters

Case	Scale	Geometry	Diameter (d)	Length (l)	Confinement	Pressure	Reynolds No.	Drag	C_D
B1	Model	Projectile	0.043 m	0.12 m	Ground-effect	1 atm	1.1 M	83.4 N	0.682
B2a	Model	Projectile	0.043 m	0.12 m	Full-tube	1 atm	1.1 M	175 N	1.44
B2b	Full	Projectile	3 m	8.45 m	Full-tube	0.001 atm	74K	888 N	1.49
B2c	Full	Pod	3 m	20 m	Full-tube	0.001 atm	74K	868 N	1.45
B2d	Full	Pod	3 m	20 m	Ground-effect	1 atm	75 M	308 kN	0.508

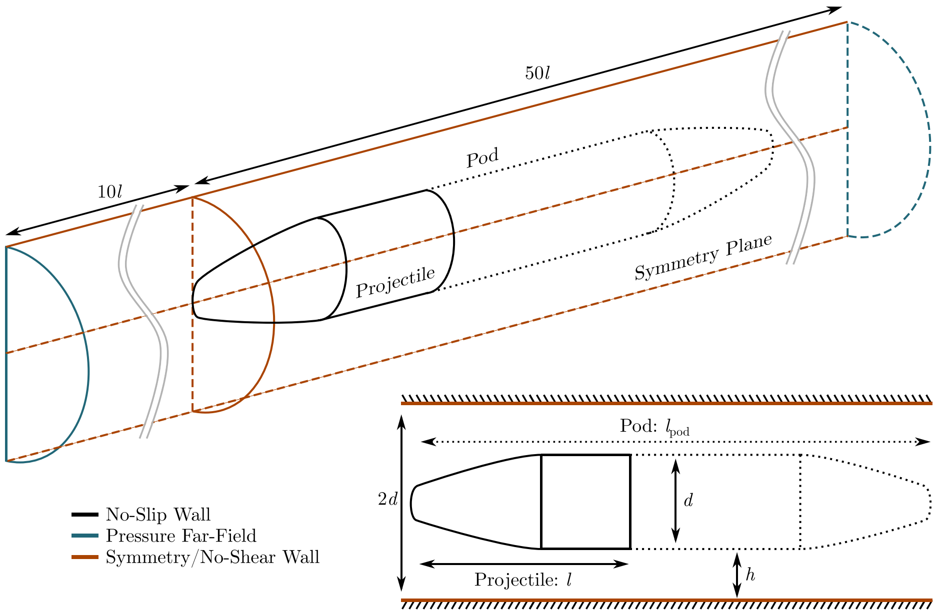

FIG. 11. Domain and boundary conditions for the Hyperloop model simulations. At model-scale, the dimensions are $d = 42.6$, $l = 120$, and $l_{pod} = 284$ mm. At full-scale $d = 3$ m, $l = 8.45$ m, and $l_{pod} = 20$ m. The blockage ratio is $\beta = 0.25$ at both scales.

Figure 13 displays Mach number contours of the flow on the symmetry plane, confirming that for a pod speed of Mach 1.1, the system is in a fully developed choked state. In this flow state, normal shocks are present upstream and downstream of the pod, which have increasing separation distance from the pod over time. For these steady-state simulations, the shocks leave the domain through the far boundaries before the simulation converges to the local steady flow. The validity of this steady modeling approach is investigated further in Sec. III E.

Exploring further, the flow exhibits expansions at the hip of the projectile and at the base corner, as seen in the Benchmark 1 case. Oblique shocks are also generated where the flow is turned back to the free-stream direction at the edge of the wake. The reflection of these shocks at the walls gives the characteristic diamond pattern, with normal shocks generated around the wake center where the reflected oblique shocks interact. The enclosed tube and associated choking of the flow cause a drag increase of 110% in comparison to the ground effect case in Benchmark 1, B1 (see Table I). This is due to a fourfold increase in drag on the nose caused by the leading normal shock and increased pressure ahead of the projectile. The nose drag becomes the dominant contribution as the change in base drag from the addition of the enclosed tube is negligible.

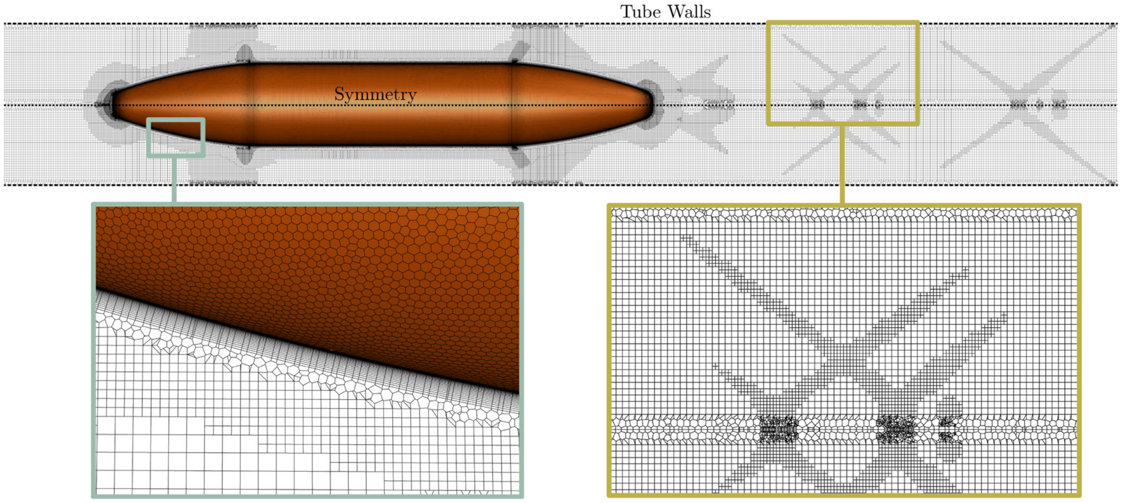

FIG. 12. Top-down view of the mesh (8.3 M cells) for the final Hyperloop simulation in the fully enclosed tube. The mesh is refined in regions with high static pressure gradients.

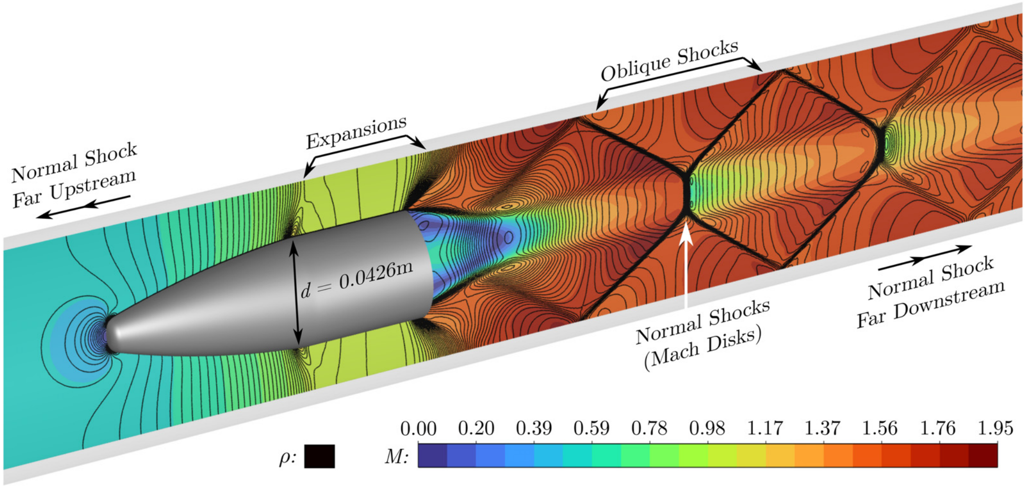

FIG. 13. Contours of Mach number and isolines of density on the symmetry plane for the model-scale projectile in tube simulation, case B2a. The projectile is at Mach 1.1 and the tube is at atmospheric pressure. The flow is choked and normal shocks are present far upstream and downstream (out of the domain).

B. Scale and operating pressure (B2b)

To perform simulations that are representative of a full-scale Hyperloop system, the entire domain was scaled up by a factor of ∼70 to give $d = 3$ and $l = 8.45$ m. This diameter is commonly used for Hyperloop simulations[2,45] and is slightly smaller than the typical size of a conventional high-speed train.[46] As the blockage ratio is kept at $\beta = 0.25$, the tube diameter is 6 m. This scale is referred to as *full-scale* in the following discussion, while the scale of the validation case (Benchmark 1) is termed *model-scale*.

In addition to changes in scale, the operating pressure of the simulation was reduced to 100 Pa. This is the value suggested by Musk,[47] and it has subsequently been taken as the default for Hyperloop simulations in the literature. The combination of the increased scale and reduced pressure is designated case B2a, and it gives a flow Reynolds number of 7.4×10^4 at Mach 1.1. This is approximately 7% of the value for the original bullet validation case, B1. A Reynolds number of 7.4×10^4 places the flow within the regime in which laminar–turbulent transition can have significant effects.[48] The transition SST turbulence model was therefore used for all of the following simulations in order to capture any influence of boundary layer transition. The Knudsen number of the flow at this reduced pressure is approximately 10^{-5}, which is still well within the regime in which the continuum approximation holds.[1,49]

The scale and operating pressure were changed simultaneously as their effect on the flow is equivalent in terms of the Reynolds number (since the pressure is proportional to density). Simulating the intermediate cases with low pressure at model-scale or atmospheric pressure at full-scale would give extreme Reynolds numbers (1000 and 75 M, respectively). These values are not representative of a Hyperloop and are outside the regime of the validated model setup, particularly with regard to turbulence modeling.

The reduction in Reynolds number had a relatively small effect on the flow characteristics, causing a drag coefficient increase of only 3% compared to the model-scale simulations at atmospheric pressure (case B2a). No appreciable changes were seen due to transition effects in this case.

C. Pod geometry (B2c)

The final modification made to the system in order to produce the Hyperloop model was a change of the body geometry. This is designated case B2c. The flat base geometry of a projectile is required for firing from a rifle; however, this creates a large wake and thus relatively high drag. A better design for a Hyperloop pod would require a tapered tail to reduce the wake size and the associated drag. To generate the pod model, the nose profile was simply reflected to produce a tapered tail, as shown in Fig. 11. The cylindrical section of the body was also extended such that the overall length of the pod was $l_{\text{pod}} = 20$ m. This is representative of sizes used in the Hyperloop literature,[50,51] though it has been shown that the length of the pod does not have a large impact on its drag coefficient.[44,45]

Contours of Mach number for this case are shown on the symmetry plane in Fig. 14. The same salient flow features are observed as in the case with the projectile in the tube (Fig. 13), albeit with a wake that is significantly narrower. Consequently, the strength of the shocks downstream of the pod is reduced due to the fact that the area outside of the wake is larger.

The drag coefficient of the pod is 1.45, a slight decrease of 2% compared to the projectile geometry, as shown in Table I. This is despite a friction drag increase of 83% caused by the significantly longer geometry of the pod. This can be explained by the fact that pressure drag is dominant in the flow, accounting for 95% of the total drag on the pod. The slight proportional decrease in pressure drag therefore outweighs the significant proportional increase in friction drag and causes an overall decrease in the total drag coefficient, compared to the projectile geometry.

D. Comparison to free air (B2d)

If the Hyperloop is to be feasible, the drag experienced by the pod in the low-pressure tube environment must be significantly lower than it would encounter in free air; otherwise, the tube and vacuum systems would be redundant. To test this, a further simulation was performed

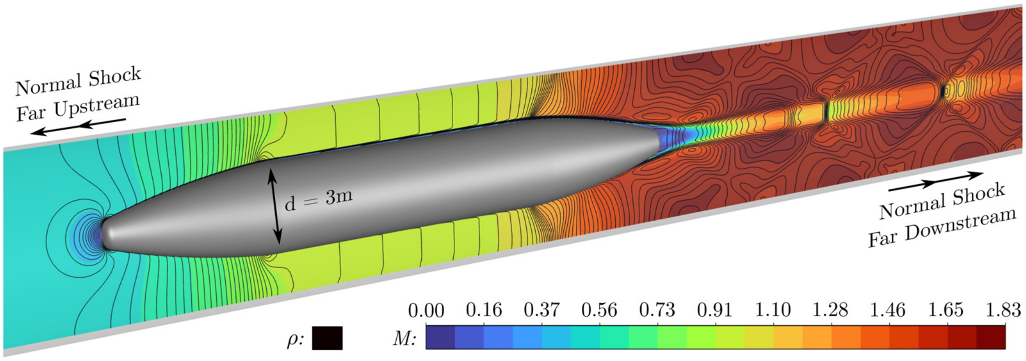

FIG. 14. Contours of Mach number and isolines of density on the symmetry plane for the full-scale Hyperloop pod model, case B2c. The pod is at Mach 1.1 and the ambient pressure in the tube is 100 Pa. The flow is choked and normal shocks are present far upstream and downstream.

using the full-scale pod geometry in ground effect at atmospheric pressure. This case is denoted as B2d.

The drag force on the pod in this free-air simulation was found to be 308 kN, while the drag in the low-pressure tube simulations was just 0.3% of this value at 868 N (Table I). This highlights that the energy used to overcome aerodynamic drag in a Hyperloop system at 100 Pa would be greatly reduced in comparison to the equivalent vehicle in free air. However, no account has been made for the energy required to produce and maintain the near-vacuum environment in the tube. This is a fundamental consideration that needs to be addressed for any feasibility analysis of the Hyperloop concept. At present, research on the vacuum component of Hyperloop is limited and accurate estimates for the associated energy consumption are not currently available.

It should be noted that the systems compared here are also highly simplified, and no attempt has been made to recreate the suspension systems and other necessary components. In practice, these are unlikely to make large differences in the relative drag of the low-pressure tube and free-air cases.

E. Transient features

If the flow in the Hyperloop system is choked, an upstream normal shock is always generated and a downstream normal shock can also be present if the speed is within the fully developed regime (recall Fig. 1). Both of these shocks move relative to the pod, with increasing separation distance over time. The simulations presented thus far have resolved the steady-state flow locally around the pod by allowing the transient normal shocks to leave the domain. To verify that this approach is an accurate simplification, a transient simulation was performed which fully resolves the motion of the shocks.

A total duration of 6 s was simulated using a fixed time step of $\mathrm{d}t = 0.004$ s. Second-order iterative time-advancement was used in the solver.[37] The transition SST turbulence model was again used and all other models, mesh sizings, and solver settings were consistent with those in the steady simulations.

The simulation was initialized with a uniform Mach 1.1 flow in the tube. Investigation of various acceleration profiles in the literature[6] suggests that this instantaneous start-up condition is acceptable for capturing the fully developed flow characteristics.

The developing flow field is shown in Fig. 15 for times $t = 0.004 - 0.28$. The leading normal shock quickly develops ahead of the pod and propagates upstream, forming a uniform flow region between the shock and the nose. The steady wake flow and shock diamond pattern is generated as the trailing normal shock disturbance travels downstream from the pod. The flow develops in the same manner as the shocks progress all the way through the tube, before leaving the domain through the far boundaries. The far-field conditions applied at the ends of the domain are designed to model shocks passing through the boundary without reflection. This is achieved by calculating the Riemann invariants (characteristics) of the flow which determine the incoming and outgoing wave properties.[34,35,52]

The drag experienced by the pod was monitored during the transient simulation and is plotted in Fig. 16. The drag coefficient converges to an approximately steady value of 1.438 after around 1 s, while the normal shocks are still within the domain. This differs by 0.8% from the value obtained in the steady simulation. After the leading shock leaves the domain, the drag coefficient increases to within 0.1% of the steady value, after which it is relatively constant. This minimal increase in C_{D} can be attributed to weak compression waves generated by the reflection of the leading shock as it exits the domain. These compressions cause a slight increase in the pressure (and therefore drag), as is highlighted by the inset plot in Fig. 16, which shows pressure at a monitor point 30 m upstream of the pod. While these reflections are not physical, their effect is minimal and the steady solution after the shocks have left the domain is a very good approximation of the local time-dependent solution. The exit of the trailing shock does not appear to have an appreciable effect on the flow.

To ensure time step independence, the flow was simulated with a halved time step of $\mathrm{d}t = 0.002$ s. The drag variation over time is also plotted in Fig. 16, showing little variation from the results using the final time step size.

The speed of the propagating normal shocks in the simulation is found to stabilize very quickly. In the pod frame of reference, the speed of the upstream and downstream shocks is measured as 96.6 and 107.3 m/s, respectively. 1D isentropic methods can also be used to predict the leading shock speed, as described by Jang *et al.*[2] This involves manipulation of the standard isentropic and normal shock equations[2,53] to form a relation between the Mach number of the upstream shock, M_{shock}, and the isentropic Mach number of the flow in the pod frame of reference, $M^{\mathrm{p}}_{\mathrm{isen}}$,

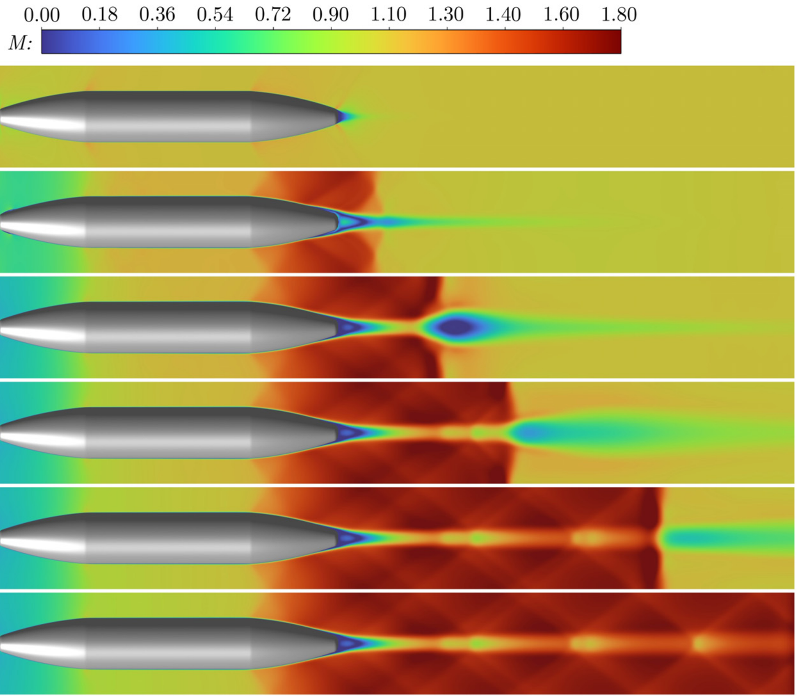

FIG. 15. Developing flow pattern at Mach 1.1 for times $t = 0.004 - 0.28$. The flow becomes locally steady after this time. Multimedia available online.

$$M_{\text{isen}}^{\text{p}} = \frac{M_{\text{shock}}[(\gamma+1)M_{\text{pod}} - 2M_{\text{shock}}]+2}{\sqrt{[2\gamma M_{\text{shock}}^2-(\gamma-1)][(\gamma-1)M_{\text{shock}}^2+2]}}, \qquad (6)$$

where γ is the specific heat ratio of the flow. This equation can be solved in combination with isentropic flow relations,[2] to find the theoretical propagation speed of the upstream shock. For this blockage ratio ($\beta = 0.25$) and pod Mach number ($M = 1.1$), the theoretical speed is calculated to be 95.5 m/s, which is within 1.1% of the simulated value.

Overall, the transient simulations have confirmed that a steady-state method can accurately reproduce the local flow around the pod in choked flow, as long as the moving shocks are allowed to leave the domain before the solution converges. Some reflection effects are seen due to interactions between the shocks and the far boundaries; however, these are minimal and do not significantly alter the flow and drag characteristics. Steady-state simulations are therefore an extremely useful tool for the rapid modeling of the flow in a Hyperloop-type system.

IV. BENCHMARK 3—HYPERLOOP IN CONFINED GROUND EFFECT (B3)

In Benchmark 2, the full-tube simulations were axisymmetric, with the pod centered within the tube. For this setup, there is no net lift force on the pod due to the symmetry. In the context of Hyperloop, it is important to consider the impact of ground effect when the pod is in close proximity to the bottom of the tube. Accordingly, a series of simulations were conducted for different ground clearances ranging from the axisymmetric case ($h = 0.5d$) down to $h = 0.05d$ (which gives a clearance of 0.15 m between the pod and the tube). To maintain generality, no attempt is made to model the suspension system of the pod, as many different systems have been proposed.[54] However, $h = 0.15$ m is within the typical range of the air gap found in maglev systems.[55] The modeling methods used in this section are consistent with those described for the steady-state simulations in Benchmark 2.

Figure 17 shows the Mach number contours on the symmetry plane for the different ground clearances. It is clear that the flow

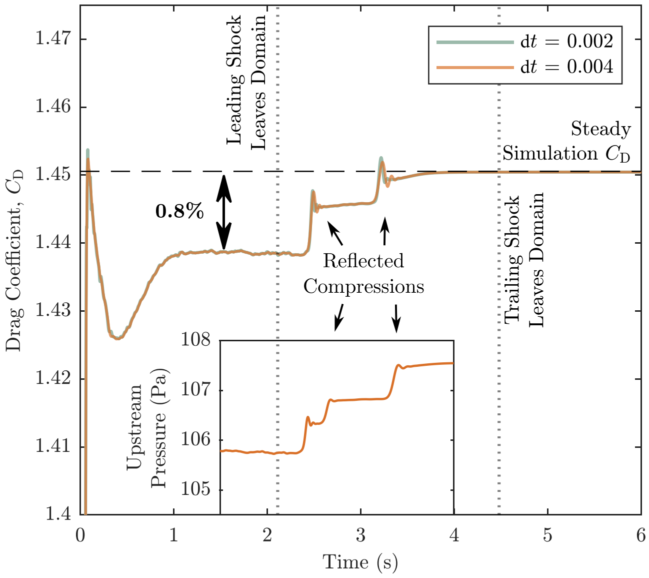

FIG. 16. Time evolution of the pod drag coefficient and the pressure at a monitor point 30 m upstream of the nose.

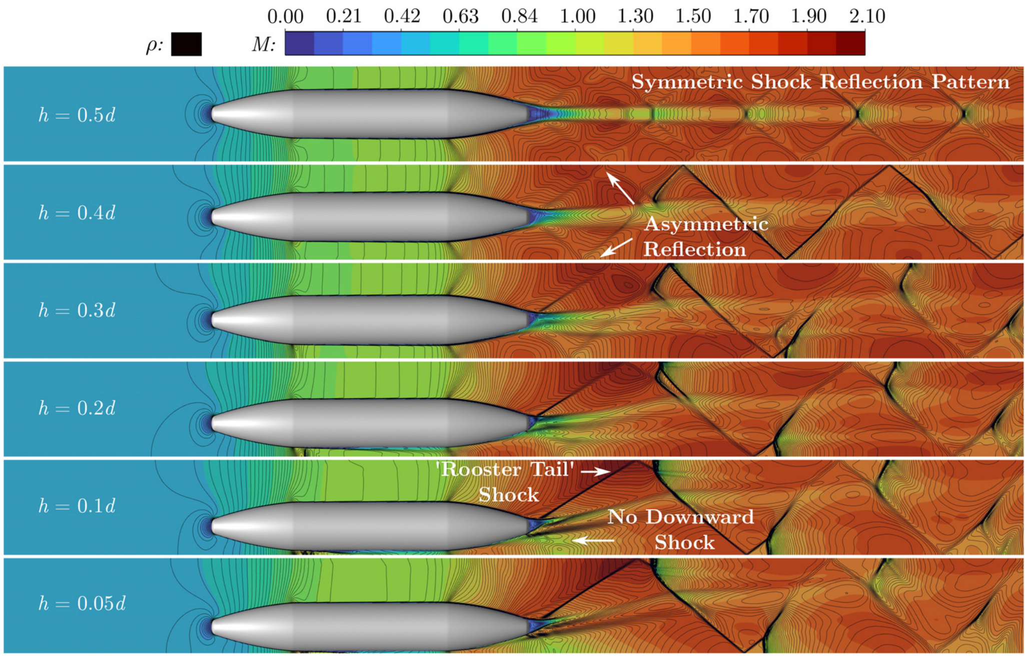

FIG. 17. Mach number contours on the symmetry plane for the various ground clearances.

upstream of the pod is insensitive to the positioning of the pod itself and remains at a uniform speed. Flow choking is dominant for all of these cases by virtue of the relatively high 25% blockage ratio. This ratio is the same for all ground clearances, irrespective of pod position, and so the choked mass flow rate past the pod is identical and the normal shock moves upstream in each case. Although not considered here, lower blockage would change the level of flow choking and thus the flow structures in the pod nose region. Moreover, the flow around the pod on the upper side is not significantly changed by the increased area when the pod sits lower in the tube. However, the flow underneath the pod is accelerated to a higher Mach number with smaller clearances, as a result of the reduced area.

With lower ground clearances, the wake of the pod is increasingly deflected upward. This is in contrast to the ground-effect cases considered in Benchmark 1, where the expansions underneath the body caused a downward deflection of the wake. The shock diamond pattern also becomes asymmetric. When the ground clearance is reduced, the oblique shock generated at the wake reflects off the wall at different lengths downstream depending on the distance to the wall. This causes a more complex shock interaction pattern as seen in Fig. 17. For the lowest clearances, no downward traveling section of the oblique shock is generated, this gives a "rooster-tail"-type geometry for the shock, which increases in strength with smaller ground separation.

Flow structures in the downstream region for the $h = 0.1d$ case are also revealed in Fig. 18. Here, total pressure contours and isosurfaces of the Q-criterion illustrate the nature of the wake structure. Two distinct trailing vortical structures are seen on either side of the symmetry plane in a similar fashion to those seen in bluff-body road vehicle aerodynamics applications. As can be seen in Fig. 18, these trailing vortices change direction, angling upward and downward in response to the predominant downstream shock direction. The initial rooster-tail shockwave is angled upward, which noticeably lifts the wake immediately behind the pod. As this shock reflects off the upper tube wall, it subsequently angles downward, which also draws the two primary vortex cores downward as well, albeit by a smaller amount. The pattern repeats itself downstream, giving rise to a shallow "saw-tooth" pathway which flattens as the intensity of both shockwaves and vorticity reduce [the predominant shock waves seen on the longitudinal centerline are overlaid on Fig. 18(b) for clarity]. This behavior is seen for all cases in close ground proximity, but it is far less evident for those with the pod close to the center of the tube. As might be expected, with the pod in the center of the tube, the wake forms a compact tube-like structure with no discernible trailing vortices. However, in the context of tube travel, close proximity to the bottom of the tube itself is the most realistic scenario.

Figure 19 shows the aerodynamic forces on the pod for the various pod positions. The drag coefficient increases as ground clearance is reduced, with the smallest clearance generating 10% higher drag than the axisymmetric case. As discussed in Secs. II F and II C, pressure drag is dominant, with the friction component only accounting for around 5% of the total drag for each of the ground clearances.

The pod experiences negative lift for all ground clearances (other than the axisymmetric case). The magnitude of this downward force also increases as the separation reduces, which is in agreement with the trend observed by Doig *et al.*[27] in their projectile results for clearances of $h/d < 0.5$. Also given in Fig. 19 is the pitching moment coefficient, C_{M_y}, of the pod for each ground clearance studied. The moment center is taken as the longitudinal midpoint along the bottom edge of the pod. This approximates the convention in train aerodynamics, in which the origin is usually defined at the top of the rails.[56] The normalization of the coefficient was based on the frontal area and height of the pod.

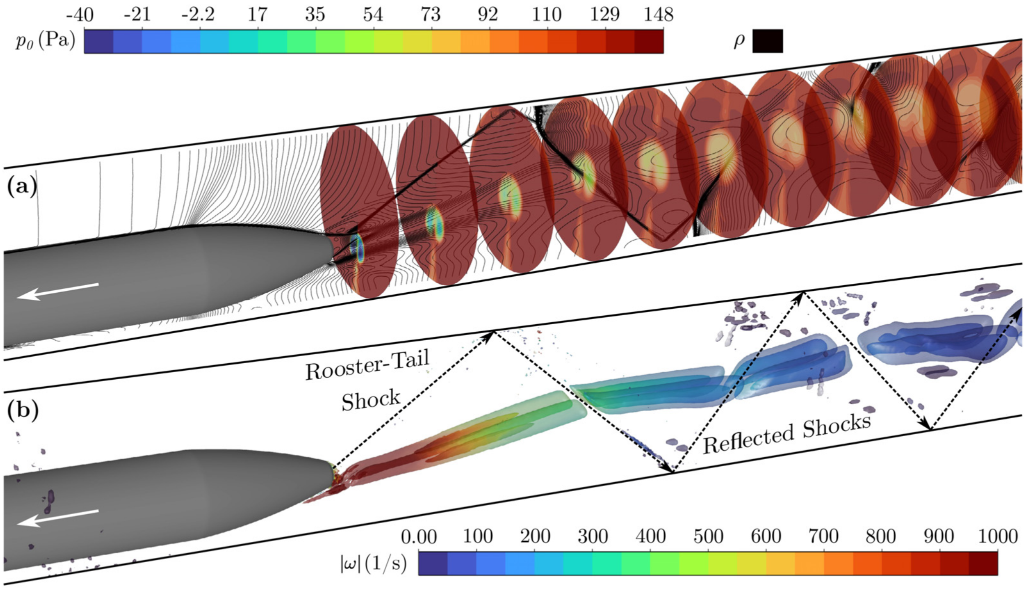

FIG. 18. (a) Total pressure contours on vertical slices through the tube along with density contours on the symmetry plane. (b) Q-criterion isosurfaces in the wake colored by vorticity magnitude. Both images show the case with ground clearance of $h = 0.1d$.

The pitching moment coefficient is observed to be positive, i.e., "nose-up," for all ground clearances. The strength of the moment also increases with lower ground separation, with the maximum at $h/d = 0.05$ being a factor of three greater than that of the pitching moment in the axisymmetric case. Again, this increase in nose-up moment with smaller clearances matches the observations in the ground effect projectile experiments.[27] A breakdown of the force contributions on each section of the pod is given in Table II for the $h/d = 0.1$ case. This highlights that the majority (70%) of the drag is due to high pressure at the nose section. Low pressure at the tail accounts for the majority of the remaining drag. Both the tail and midsection of the pod experience overall negative lift (i.e., downforce), while a smaller positive lift is observed at the nose section. This gives the total negative lift force on the pod and the positive pitching moment about the bottom center point.

Coefficients of surface pressure and skin friction in the streamwise (x) direction are plotted in Fig. 20 for $h = 0.1d$ and $h = 0.5d$ (axisymmetric case). As expected, the pressure profile on the nose and mid-sections of the pod are similar to those of the projectile (Benchmark 1) due to the shared geometry. The pressure decrease remains linear over the rest of the mid-section before dropping rapidly and becoming negative at the transition to the tail section. The

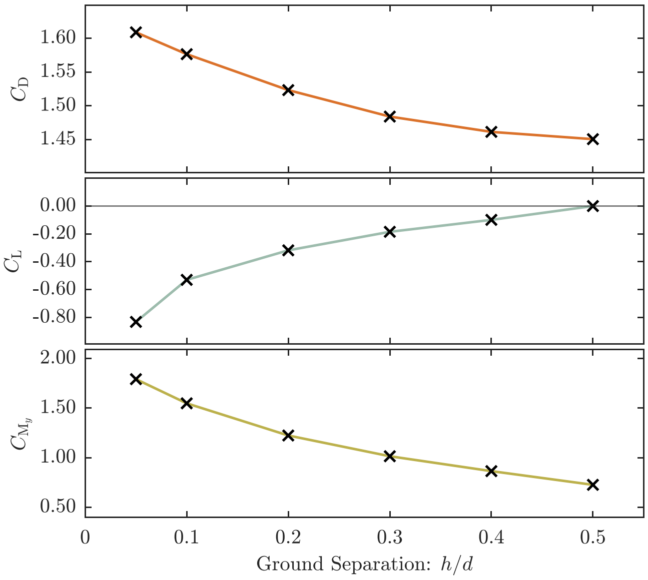

FIG. 19. Drag coefficient, C_D, lift coefficient, C_L, and pitching moment coefficient, C_{M_y}, for the pod with varying ground clearance. The moment center is taken as the lengthwise midpoint at the bottom edge of the pod.

TABLE II. Lift and drag coefficient contributions by zone on the pod for the ground clearance of $h = 0.1d$.

Zone		C_D	C_L
Nose	Lower	0.556	1.510
	Upper	0.519	−1.396
	Total	1.074	0.114
Midsection	Lower	0.015	1.307
	Upper	0.015	−1.592
	Total	0.030	−0.285
Tail	Lower	0.273	−0.769
	Upper	0.199	0.409
	Total	0.472	−0.360
Net		1.576	−0.530

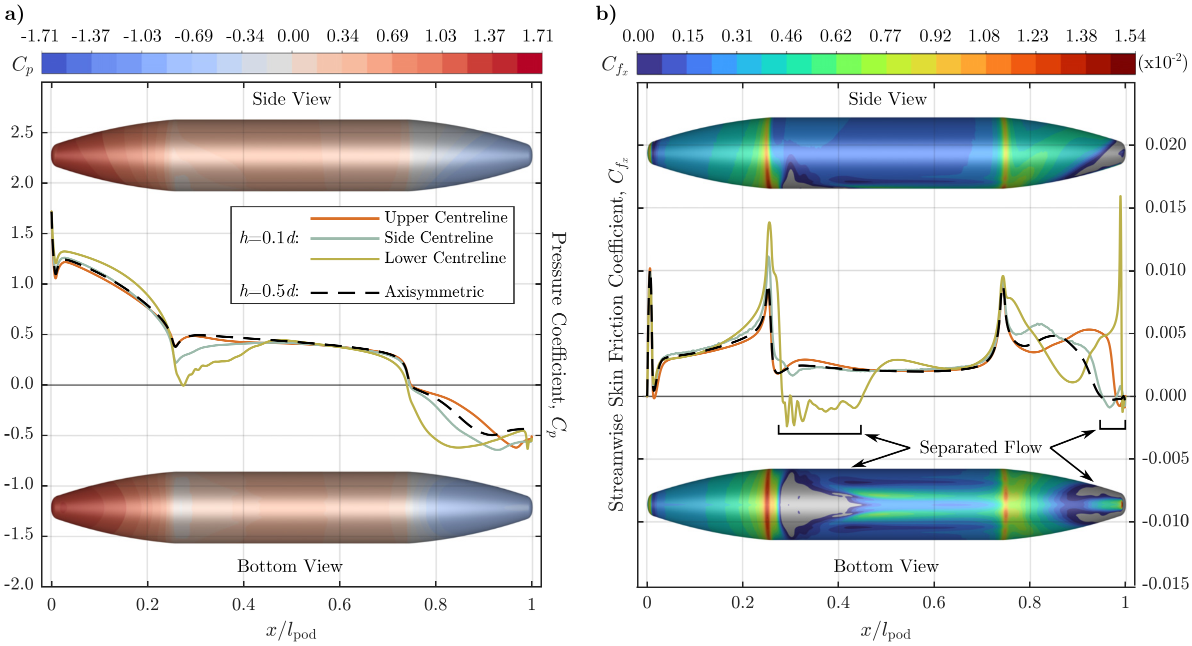

FIG. 20. (a) Surface pressure coefficient and (b) skin friction coefficient in the streamwise (x) direction. The contours show the results on the full pod surface for the $h = 0.1d$ case. The line plots show the results on the upper, side, and lower centerlines of the pod for $h = 0.1d$, along with an axisymmetric centerline for $h = 0.5d$. Negative values of streamwise skin friction, which correspond to regions of separated flow, are shown in gray.

pressure profile in the axisymmetric case is similar to that of the upper surface for the pod with lower ground clearance. However, the pressure profile is significantly altered on the underside, with the smaller ground clearance causing lower pressure areas both at the transition section around $x/l = 0.25$ and over the full tail section.

The areas of highest skin friction are observed near the very ends of the pod and in the sections where the geometry transitions between the straight body and the curved nose/tail sections. These areas correspond to where the curvature of the geometry is highest [recall Fig. 5(a)]. Areas of negative streamwise skin friction are highlighted in Fig. 20, as this gives the regions in which the boundary layer is separated and the flow is reversed. A notable separated region is seen on the underside of the pod for the case $h = 0.1d$, just after the high curvature section and where the flow becomes restricted. This separation is only seen for the ground clearances of $h = 0.2d$ and below. Smaller separated regions are also present toward the back of the tail for all ground clearances, which mark the onset of the wake structure. The total area of the separated flow regions increases with lower ground clearances, from 2.5% of the overall pod surface at $h = 0.5d$ to 6.3% at $h = 0.05d$.

V. DISCUSSION AND CONCLUSIONS

The flow characteristics of a Hyperloop system are complex due to the transonic speeds and confined tube environment. In the literature, CFD has been used extensively to simulate these systems, which has allowed for advances in the understanding of the fundamental aerodynamic characteristics expected in a Hyperloop system.

The difficulties associated with creating the appropriate Hyperloop flow conditions have meant that very little experimental research has been conducted to date. Therefore, numerical results are typically validated with empirical data from related applications. A transonic projectile in ground effect is suggested here as a validation case (Benchmark 1) that is more appropriate than others found in the literature. This system is in the appropriate Mach number regime and also incorporates wall confinement and the associated shock reflection effects.

Extending this approach, Benchmark 2 is proposed, which accounts for changes in geometry to produce a baseline pod within a tube, as well as realistic scale and operating conditions. Finally, Benchmark 3 accounts for ground clearance effects. As detailed in this paper, the process of developing Benchmark 1 and extending this to Benchmark 3 involved a number of steps. Key observations at each stage can be summarized as follows.

1. A CFD method has been successfully used to simulate the flow generated by a projectile traveling at Mach 1.1 in free air and with a ground clearance of $h = 0.5d$. The simulated pressure profiles on the pod show good agreement with those obtained by Doig *et al.*[27] in wind tunnels tests. Qualitative comparison to the flow fields in wind tunnel and live firing experiments also show that the CFD approach is able to accurately capture the correct shock reflection and interaction characteristics.
2. Changing the wall confinement from a ground plane to a fully enclosed tube has a significant effect on the flow characteristics. Most notably, flow choking is possible and was observed at the conditions used here (Mach 1.1, 25% blockage). This causes moving normal shocks to be generated upstream and

downstream of the pod and a sharp increase of 110% in the drag coefficient.

3. Increasing scale to a 6 m tube and decreasing the ambient pressure to 100 Pa combined to give a Reynolds number reduction to 7.4×10^4 (7% of the value in Benchmark 1). This had a small effect on the drag coefficient, which increased by only 3%. Converting to a more realistic Hyperloop geometry by lengthening the pod and making a symmetric nose/tail caused a slight (2%) decrease in drag coefficient. This is due to the fact that pressure drag is dominant, with friction drag only accounting for around 5% of the total. The pressure drag is very similar between the two geometries due to the consistent blockage ratio and the shared nose shape.
4. In comparison to the equivalent full-scale, free-air system, the pod in the low air-density tube experiences only 0.3% of the drag force. The simulated Hyperloop-type system is therefore achieving the intended benefit of significantly reduced drag, which would in turn reduce energy consumption. However, this does not include any consideration of the energy used in generating and maintaining the partial vacuum environment.
5. By comparing to transient simulations, it is found that a steady-state approach is appropriate for simulating choked flow in a Hyperloop system. In order for the steady simulations to converge, the moving normal shocks can be allowed to leave the domain through characteristic-type boundary conditions, which model the passing of the waves without generating significant reflections. The flow around the pod in the region between the upstream and downstream normal shocks is found to be steady.
6. Lowering the ground clearance of the pod breaks the axisymmetry of the simulations, causing the wake of the pod to be deflected upward and the symmetric shock pattern to be disrupted. The drag and downward force increase with lowering ground clearance, as does the nose-up pitching moment. Flow separation also occurs underneath the pod for lower ground clearances.

In addition to these specific observations, some more general comments are discussed here. The work presented in this paper was based on the widely used SST $k-\omega$ turbulence model[24] and, for the lower Reynolds number cases, the transition SST model.[40] It is important to appreciate that turbulence modeling continues to develop. Alternative RANS formulations and the higher fidelity of Scale-Resolving Simulation (SRS) approaches could improve the predictions of confined transonic flow such as those encountered in Hyperloop systems. Therefore, an open mind should be kept by practitioners in this field.

To conclude, this paper proposes three benchmark cases that can be used to compare other computational approaches for simulating choked flow in a Hyperloop system. All of the output data from this study are available for the purpose of benchmarking other codes and modeling approaches. In particular, high-fidelity simulations of these cases, using methods such as Large Eddy Simulation (LES), would give further insight into the characteristics of the flow. This would allow further assessment of the reliability of RANS methods for modeling the transonic choked aerodynamics. Ultimately, these benchmarks will also be useful for comparing to experimental data when this is obtained by the research community.

Future work on these benchmark cases should also include a study on Mach number and blockage ratio effects, as these parameters have been identified as the determining factors for the flow states in a Hyperloop (see Fig. 2). Simulating the feasible range of both parameters will therefore capture the characteristics of the system across the full design-space.

Thinking beyond these specific observations, the pod design proposed in this paper is relatively simple, making it straightforward to test using other simulation approaches. With bullet-inspired origins and supporting experimental data, this is a sensible starting point for other researchers to develop simulations which contain the expected aerodynamic characteristics. An important point to appreciate is that that the pod shape in question is a starting point for future design iterations. It is envisaged that newer designs, adapted to the unique demands of the Hyperloop environment, will follow; the pod shape proposed is by no means ideal, and there is significant scope for aerodynamic shape optimization.

ACKNOWLEDGMENTS

This work was supported by the UK Engineering and Physical Sciences Research Council (EPSRC) Grant No. EP/S022732/1 for the University of Leeds Centre for Doctoral Training in Fluid Dynamics. This work was undertaken on ARC3/4, part of the High Performance Computing facilities at the University of Leeds, UK. The authors thank Graham Doig and Harald Kleine for providing details of their experiments to aid the setup of the numerical validation.

AUTHOR DECLARATIONS

Conflict of Interest

The authors have no conflicts to disclose.

Author Contributions

Alex J. Lang: Conceptualization (equal); Investigation (equal); Methodology (equal); Writing – original draft (equal). **David P. Connolly:** Supervision (equal); Writing – review & editing (equal). **Gregory de Boer:** Supervision (equal); Writing – review & editing (equal). **Shahrokh Shahpar:** Supervision (equal); Writing – review & editing (equal). **Benjamin Hinchliffe:** Supervision (equal); Writing – review & editing (equal). **Carl A. Gilkeson:** Project administration (equal); Resources (equal); Supervision (equal); Writing – original draft (equal); Writing – review & editing (equal).

DATA AVAILABILITY

The data that support the findings of this study are openly available in a dataset at doi.org/10.5281/zenodo.11261349.

REFERENCES

[1] A. J. Lang, D. P. Connolly, G. de Boer, S. Shahpar, B. Hinchliffe, and C. A. Gilkeson, "A review of Hyperloop aerodynamics," Comput. Fluids **273**, 106202 (2024).

[2] K. S. Jang, T. T. G. Le, J. Kim, K. S. Lee, and J. Ryu, "Effects of compressible flow phenomena on aerodynamic characteristics in Hyperloop system," Aerosp. Sci. Technol. **117**, 106970 (2021).

[3] Z. Hou, Y. Zhu, J. Bo, and J. Yang, "A quasi-one-dimensional study on global characteristics of tube train flows," Phys. Fluids **34**, 26104 (2022).

[4] Q. Yu, X. Yang, J. Niu, Y. Sui, Y. Du, and Y. Yuan, "Aerodynamic thermal environment around transonic tube train in choked/unchoked flow," Int. J. Heat Fluid Flow **92**, 108890 (2021).
[5] Y. Sui, Q. Yu, J. Niu, X. Cao, X. Yang, and Y. Yuan, "Flow characteristics and aerodynamic heating of tube trains in choked/unchoked flow: A numerical study," J. Therm. Sci. **32**, 1421–1434 (2023).
[6] H. Bi, Z. Wang, H. Wang, and Y. Zhou, "Aerodynamic phenomena and drag of a maglev train running dynamically in a vacuum tube," Phys. Fluids **34**, 096111 (2022).
[7] J. Niu, Y. Sui, Q. Yu, X. Cao, Y. Yuan, and X. Yang, "Effect of acceleration and deceleration of a capsule train running at transonic speed on the flow and heat transfer in the tube," Aerosp. Sci. Technol. **105**, 105977 (2020).
[8] H. Kim and S. Oh, "Shape optimization of a hyperloop pod's head and tail using a multi-resolution morphing method," Int. J. Mech. Sci. **223**, 107227 (2022).
[9] T. T. G. Le, J. Kim, M. Cho, and J. Ryu, "Effects of tail shapes/lengths of Hyperloop pod on aerodynamic characteristics and wave phenomenon," Aerosp. Sci. Technol. **131**, 107962 (2022).
[10] T. T. G. Le, J. Kim, K. S. Jang, K. S. Lee, and J. Ryu, "Numerical study on the influence of the nose and tail shape on the aerodynamic characteristics of a Hyperloop pod," Aerosp. Sci. Technol. **121**, 107362 (2022).
[11] Y. Seo, M. Cho, D. H. Kim, T. Lee, J. Ryu, and C. Lee, "Experimental analysis of aerodynamic characteristics in the Hyperloop system," Aerosp. Sci. Technol. **137**, 108265 (2023).
[12] N. Li, J. T. Chang, K. J. Xu, D. R. Yu, W. Bao, and Y. P. Song, "Prediction dynamic model of shock train with complex background waves," Phys. Fluids **29**, 116103 (2017).
[13] B. U. Reinartz, C. D. Herrmann, J. Ballmann, and W. W. Koschel, "Aerodynamic performance analysis of a hypersonic inlet isolator using computation and experiment," J. Propul. Power **19**, 868–875 (2003).
[14] C. D. Herrmann and W. W. Koschel, "Experimental investigation of the internal compression of a hypersonic intake," AIAA Paper No. AIAA 2002-4130, 2002.
[15] R. Guerra, W. Waidmann, and C. Laible, "An experimental investigation of the combustion of a hydrogen jet injected parallel in a supersonic air stream," AIAA Paper No. AIAA 1991-5102, 1991.
[16] W. Waidmann, F. Alff, U. Brummund, W. Clauss, M. Oschwald, J. Sender, and W. Waidmann, "Experimental investigation of the combustion process in a supersonic combustion ramjet (SCRAMJET) combustion chamber," in *Deutscher Luft- Und Raumfahrtkongress* (DGLR-Jahrestagung, 1994).
[17] T. Gao, J. Liang, M. Sun, and Y. Zhao, "Analysis of separation modes variation in a scramjet combustor with single-side expansion," AIAA J. **55**, 1307 (2017).
[18] S. Saito, M. Iida, and H. Kajiyama, "Numerical simulation of 1-D unsteady compressible flow in railway tunnels," J. Environ. Eng. **6**, 723 (2011).
[19] H. A. Stine, K. Wanlass, M. Field, and C. Washington, "Theoretical and experimental investigation of aerodynamic-heating and isothermal heat-transfer parameters on a hemispherical nose with laminar boundary layer at supersonic Mach numbers," Report No. NACA-TN-3344 (NACA, 1954).
[20] X. Hu, Z. Deng, J. Zhang, and W. Zhang, "Effect of tracks on the flow and heat transfer of supersonic evacuated tube maglev transportation," J. Fluids Struct. **107**, 103413 (2021).
[21] X. Hu, Z. Deng, and W. Zhang, "Effect of cross passage on aerodynamic characteristics of super-high-speed evacuated tube transportation," J. Wind Eng. Ind. Aerodyn. **211**, 104562 (2021).
[22] L. D. Kayser and F. Whiton, "Surface pressure measurements on a boattailed projectile shape at transonic speeds," Technical Report No. ARBRL-MR-03161 (US Army Armament Research And Development Command, 1982).
[23] R. Hruschka and D. Klatt, "In-pipe aerodynamic characteristics of a projectile in comparison with free flight for transonic Mach numbers," Shock Waves **29**, 297–306 (2019).
[24] F. R. Menter, "Two-equation eddy-viscosity turbulence models for engineering applications," AIAA J. **32**, 1598–1605 (1994).
[25] G. Doig, "Transonic and supersonic ground effect aerodynamics," Prog. Aerosp. Sci. **69**, 1–28 (2014).
[26] G. Doig, T. J. Barber, E. Leonardi, A. J. Neely, and H. Kleine, "Aerodynamics of a supersonic projectile in proximity to a solid surface," AIAA J. **48**, 2916–2930 (2010).
[27] G. Doig, S. Wang, H. Kleine, and J. Young, "Aerodynamic analysis of projectiles in ground effect at near-sonic Mach numbers," AIAA J. **54**, 150–160 (2016).
[28] J. Young, K. Carriage, B. Oakes, H. Kleine, K. Hiraki, and Y. Inatani, "Numerical simulation and experiments on the ground effect of transonic projectiles," in *29th International Symposium on Shock Waves 2* (Springer International, 2015), pp. 1297–1302.
[29] H. Kleine, J. Young, B. Oakes, K. Hiraki, H. Kusano, and Y. Inatani, "Aerodynamic ground effect for transonic projectiles," in *28th International Symposium on Shock Waves* (Springer-Verlag Berlin, Heidelberg, 2012), pp. 519–524.
[30] C. Sheridan, J. Young, H. Kleine, K. Hiraki, and S. Nonaka, "Ground effect of transonic and supersonic projectiles: Influence of Mach number and ground clearance," in *Proceedings of the 30th International Symposium on Shock Waves 1* (Springer International Publishing AG, 2017), pp. 635–640.
[31] H. Kleine and H. Grönig, "Color schlieren methods in shock wave research," Shock Waves **1**, 51–63 (1991).
[32] J. B. Barlow, W. H. Rae, and A. Pope, *Low-Speed Wind Tunnel Testing*, 3rd ed. (Wiley & Sons, 1999).
[33] G. C. Doig, T. J. Barber, E. Leonardi, A. J. Neely, and H. Kleine, "Methods for investigating supersonic ground effect in a blowdown wind tunnel," Shock Waves **18**, 155–159 (2008).
[34] ANSYS Fluent User's Guide, Release 2020R2 (Ansys, Inc, Canonsburg, PA, 2020).
[35] F. Moukalled, L. Mangani, and M. Darwish, "The characteristic boundary condition in pressure-based methods," Numer. Heat Transfer, Part B **76**, 43–59 (2019).
[36] W. Sutherland, "The viscosity of gases and molecular force," London, Edinburgh, Dublin Philos. Mag. J. Sci. **36**, 507–531 (1893).
[37] ANSYS Fluent, Commercial CFD Software Package, Ver. 2020R2 (Ansys, Inc, Canonsburg, PA, 2020).
[38] H. K. Versteeg and W. Malalasekera, *An Introduction to Computational Fluid Dynamics*, 2nd ed. (Pearson, 2007).
[39] M. Drela, "XFOIL: An analysis and design system for low Reynolds number airfoils," in *Low Reynolds Number Aerodynamics, Proceedings of the Conference Notre Dame, Indiana, 5–7 June* (Springer, Berlin, Heidelberg, 1989).
[40] F. R. Menter, R. B. Langtry, S. R. Likki, Y. B. Suzen, P. G. Huang, and S. Völker, "A correlation-based transition model using local variables—Part I: Model formulation," J. Turbomach. **128**, 413–422 (2006).
[41] R. B. Langtry, F. R. Menter, S. R. Likki, Y. B. Suzen, P. G. Huang, and S. Völker, "A correlation-based transition model using local variables—Part II: Test cases and industrial applications," J. Turbomach. **128**, 423–434 (2006).
[42] R. B. Langtry and F. R. Menter, "Transition modeling for general CFD applications in aeronautics," AIAA Paper No. AIAA 2005-522, 2005.
[43] Z. Zhou, C. Xia, X. Du, X. Shan, and Z. Yang, "Impact of the isentropic and Kantrowitz limits on the aerodynamics of an evacuated tube transportation system," Phys. Fluids **34**, 066103 (2022).
[44] J. S. Oh, T. Kang, S. Ham, K. S. Lee, Y. J. Jang, H. S. Ryou, and J. Ryu, "Numerical analysis of aerodynamic characteristics of Hyperloop system," Energies **12**, 518 (2019).
[45] T. T. G. Le, K. S. Jang, K.-S. Lee, and J. Ryu, "Numerical investigation of aerodynamic drag and pressure waves in Hyperloop systems," Mathematics **8**, 1973 (2020).
[46] U.S Department of Transportation, "Aerodynamic assessment and mitigation—Design considerations for high-speed rail," Report No. 20590 (U.S Department of Transportation, 2022).
[47] Musk, E., "Hyperloop alpha" (2013), https://tesla.com/sites/default/files/blog_images/hyperloop-alpha.pdf, retrieved 10 September 2024.
[48] P. B. S. Lissaman, "Low-Reynolds-number airfoils," Annu. Rev. Fluid Mech. **15**, 223–239 (1983).
[49] M. A. Saad, *Compressible Fluid Flow* (Prentice-Hall Inc., 1985).
[50] J. Niu, Y. Sui, Q. Yu, X. Cao, and Y. Yuan, "Numerical study on the impact of Mach number on the coupling effect of aerodynamic heating and aerodynamic pressure caused by a tube train," J. Wind Eng. Ind. Aerodyn. **190**, 100–111 (2019).

[51] Y. Sui, J. Niu, P. Ricco, Y. Yuan, Q. Yu, X. Cao, and X. Yang, "Impact of vacuum degree on the aerodynamics of a high-speed train capsule running in a tube," Int. J. Heat Fluid Flow **88**, 108752 (2021).

[52] M. M. Alloush, F. Moukalled, L. Mangani, and M. Darwish, "An implicit implementation of the characteristic boundary condition in a fully coupled pressure-based flow solver," Numer. Heat Transfer, Part B **78**, 330–347 (2020).

[53] TRUN "REJ. D. Anderson, *Fundamentals of Aerodynamics*, 6th ed. (McGraw-Hill, 2016).

[54] E. Chaidez, S. P. Bhattacharyya, and A. N. Karpetis, "Levitation methods for use in the hyperloop high-speed transportation system," Energies **12**, 4190 (2019).

[55] H. W. Lee, K. C. Kim, and J. Lee, "Review of Maglev train technologies," IEEE Trans. Magn. **42**, 1917–1925 (2006).

[56] C. Baker, T. Johnson, D. Flynn, H. Hemida, A. Quinn, D. Soper, and M. Sterling, *Train Aerodynamics: Fundamentals and Applications* (Butterworth-Heinemann, 2019).